# Evaluation of the use of wavefront encoding to reduce depth-induced aberration in structured illumination microscopy

Nurmohammed Patwary[a], Jorge Sola-Pikabea[b], Ana Doblas[a], Genaro Saavedra[b], Manuel Martinez-Corral[b], Chrysanthe Preza[a*]
[a]Dept. of Electrical and Computer Engineering, the Univ. of Memphis, TN 38152, USA
[b]Dept. of Optics, Univ. of Valencia, Burjassot, Spain

## ABSTRACT

Three-dimensional imaging is affected by depth-induced spherical aberration (SA) when imaging deep into an optically thick sample. In this work, we evaluate the impact of SA on the performance of incoherent grating-projection structured illumination microscopy (SIM). In particular, we analyze the reduction of the contrast in the structured pattern and compare the reconstructed SIM images for different amounts of SA. In order to mitigate the impact of SA, we implement and evaluate in SIM a wavefront encoded imaging system using a square cubic (SQUBIC) phase mask, an approach shown previously to be successful in conventional microscopy.

**Keywords:** Spherical aberration, wavefront encoding, fluorescence microscopy, structured illumination microscopy.

## 1. INTRODUCTION

Three-dimensional (3D) imaging of optically thick samples is perturbed due to the presence of depth-induced spherical aberration (SA). This effect is well known for widefield (WF) fluorescence microscopy and different techniques [1-3] have been proposed to address it in the last decades. One of the techniques used to reduce the SA impact is wavefront encoding (WFE). WFE is based on the modification of the conventional point spread function (PSF) by inserting a phase mask (PM) [4-7] at the aperture stop of the microscope objective (MO) lens [8], which provides an engineered WFE-PSF that is more insensitive to SA. In Refs. [6, 7], a radially-symmetric squared cubic (SQUBIC) PM [5] was evaluated to reduce SA variability in both simulation and experiment.

In this paper, the effect of depth-induced aberration has been evaluated in a commercially-available SIM system, in which modulation fringes are generated by the incoherent projection of an illumination linear grating (Zeiss ApoTome® SIM). In earlier studies [9, 10], authors presented results of their initial investigation on the impact of SA on the images provided by this grating projection SIM (pSIM) system. Here, we continue this study and also evaluate the use of SQUBIC-WFE with the pSIM in order to improve the restored images in presence of depth-induced SA. Particularly, the impact of SA on conventional pSIM images and SQUBIC-WFE pSIM images are evaluated in both simulation and experiment by restoring images of a test object from different depth locations below the cover slip. The paper is organized as follows. Section 2 describes the basic theory of SIM. The methodologies used in the investigation are described in Section 3. Section 4 is devoted to discussion of simulated and experimental results. Finally, the main findings are summarized in Section 5.

## 2. BACKGROUND

### 2.1 Conventional pSIM

The pSIM forward imaging model was developed in [11, 12] assuming space-invariant imaging, which was further modified to address the depth-induced SA [9, 10]. This model was later extended to account the effect of depth-variant (DV) SA [12, 13]. The DV forward SIM model uses multiple DV PSFs computed at different depth locations and computes the raw SIM image using a superposition integral instead of a convolution [12]. In this paper, we use the space-invariant imaging model and a single aberrant PSF at a particular imaging depth to account for DV SA. This is an approximation, which is valid if the object is axially confined at a particular depth (as is the case of the numerical objects and test samples used in the studies presented here).

* cpreza@memphis.edu; Phone: 1-(901) 678-4369, Fax: 1-(901) 678-5469

Three-Dimensional and Multidimensional Microscopy: Image Acquisition and Processing XXV, edited by Thomas G. Brown, Carol J. Cogswell, Tony Wilson, Proc. of SPIE Vol. 10499, 104991A

In pSIM systems, the 3D illumination pattern is produced by the incoherent projection of a linear grating onto the object plane. This source presents an irradiance distribution which is mathematically represented by

$$s_i(\mathbf{x}) = \delta(z)\ \left[1+\cos(2\pi f_M x+\varphi_i)\right],\quad i=1,2,....N, \tag{1}$$

where $\boldsymbol{x}=(x,y,z)$, $\delta(z)$ is the Dirac delta function, and $f_M$ and $\varphi_i$ are the modulation frequency and the phase shifting of the illumination fringes, respectively, and $N \geq 3$ is the number of phase-shifted structured patterns. The corresponding $N$ forward (raw) pSIM images at an imaging depth $d$ below the cover slip are described by [9-11]

$$g_i(\mathbf{x};d) = o(\mathbf{x}) \otimes_3 h_D(\mathbf{x};d) + m_c\left[o_c(\mathbf{x})\cos(\varphi_i)+o_s(\mathbf{x})\sin(\varphi_i)\right]\otimes_3 h_{SIM}(\mathbf{x};d), \tag{2}$$

where $\otimes_3$ is the 3D convolution operator, $m_c$ is a constant for the modulation contrast, $h_D(\mathbf{x};d)$ is the detection PSF, $o_c(\mathbf{x}) = o(\mathbf{x})\cos(2\pi f_M\ x)$ and $o_s(\mathbf{x}) = -o(\mathbf{x})\sin(2\pi f_M\ x)$, are the cosine and sine component, respectively, and

$$h_{SIM}(\mathbf{x};d) = h_D(\mathbf{x};d)\ m\left(z;f_M,d\right), \tag{3}$$

is the synthetic pSIM-PSF at a depth $d$ below the coverslip, where

$$m(z;f_M,d) = \int \cos(2\pi f_M\ x_0)\ \left(\int h_I(x_0,y_0,z;d)\ \mathrm{d}\,y_0\right)\ \mathrm{d}\,x_0 \tag{4}$$

is the axial modulation function, being $h_I(\mathbf{x};d)$ the PSF corresponding to the illumination system. It is important to realize that the axial modulation function depends on the modulation frequency and the depth of the object. The $m(z;f_M,d)$ function extends axially with the increase of SA, and becomes narrower with the increase of the modulation frequency $f_M$.

### 2.2 SQUBIC-WFE pSIM

In the case of SQUBIC-WFE pSIM system, since SQUBIC is introduced in the detection imaging path the forward image can still be computed using Eq. (2) but taking into account that the detection PSF needs to be replaced by the SQUBIC PSF, $h_{SQUBIC}(\mathbf{x};d)$ [7]. Note that this change also affects the synthetic SIM-PSF of Eq. (3). The most significant drawback in the SQUBIC-WFE pSIM raw images is that their modulation contrast is significantly penalized. In pSIM, the modulation contrast ($m_c$) of the structured pattern at the image plane of the objective lens can be expressed as the square modulus of the 2D detection optical transfer function (OTF), which is the Fourier transform of the detection PSF at the best focal (*bf*) plane, $m_c = \left|H_{D,bf}(f_M,0;d)\right|^2$. Here we have assumed that the illumination and detection PSFs are the same. However, for SQUBIC-WFE pSIM imaging the modulation contrast of the fringes is reduced by the 2D SQUBIC OTF. Thus, $m_c = \left|H_{D,bf}(f_M,0;d)\times H_{SQUBIC,bf}(f_M,0;d)\right|$, whose effective compact support is narrower [13].

## 3. METHODS

All the simulations were carried out in Matlab (MathWorks®, Natica, MA). To compute the WF-PSFs we used the Gibson & Lanni optical path distance model [14] on a 128 × 128 × 256 grid with a voxel dimension of 0.05 μm$^3$. PSFs for a 63×/1.4 NA oil (RI = 1.518) immersion objective lens was computed using an emission wavelength equal to 515 nm and assuming a sample embedding medium refractive index (RI) equal to 1.47. The synthetic pSIM-PSFs were computed using Eq. (3) in which the function $m(z;f_M,d)$ was calculated by means of Eq. (4) using $f_M = 0.09f_c$, where is the cutoff frequency of the MO. Simulated images were computed using Eq. (2), which requires both the WF-PSF and the synthetic pSIM-PSF. The SQUBIC-WFE PSFs for pSIM and noisy images were computed using the methods described in Section 2 of Ref. [6].

To match the experimental conditions, a 63×/1.4 NA oil immersion objective lens with the "M"-illumination grating (the modulation frequency is equal to $f_M = 0.09f_c = 0.45$ μm$^{-1}$) was simulated. The test object used in this study is a 6 μm in diameter spherical shell with a shell thickness equal to 1 μm, and the refractive index (RI) of the specimen embedding medium is equal to 1.47, which is the RI of the sample mounting medium used in the experiment. The emission wavelength and the voxel dimension is 515 nm, and 0.1 μm$^3$, respectively.

The experimental implementation of the SQUBIC-WFE pSIM imaging system is shown in Fig. 1, which shows the SQUBIC-WFE path implemented in the side imaging-path of a Zeiss AxioImage.1® microscope, and the ApoTome® slider

that creates the illumination pattern. For the SQUBIC-WFE path, we have used a customized phase mask. More technical details of the experimental setup and sample preparation methods are discussed in Ref. [6].

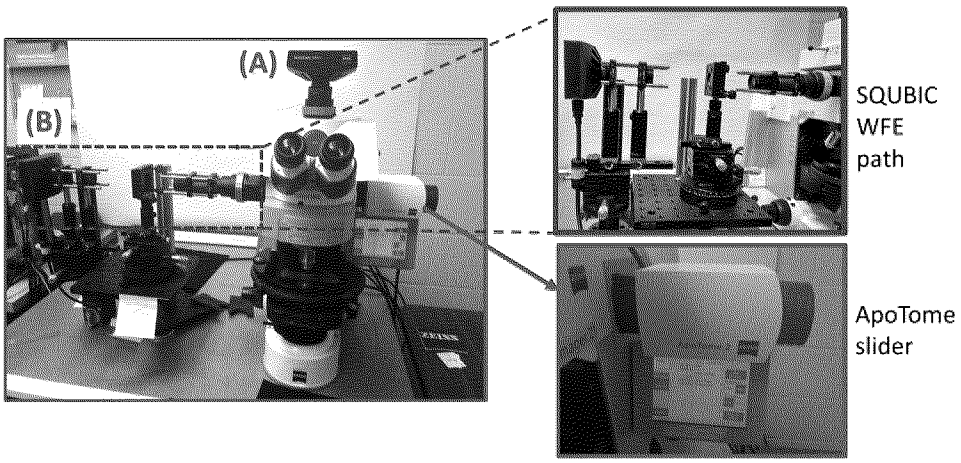


Fig. 1: Experimental implementation of the SQUBIC-WFE pSIM imaging system. In this setup, the conventional ApoTome® SIM images are captured from the top imaging path (camera A), and the SQUBIC-WFE pSIM images are captured from the side imaging path (camera B).

# 4. RESULTS

## 4.1 Effect of depth-induced SA on pSIM in simulation

To investigate the effect of depth-induced SA on the conventional pSIM imaging, we simulated images of a 6-μm spherical shell over a 100 μm depth (SNR=27 dB). For a comparative study, we also simulated the corresponding WF images of this test object. Fig. 2 (a) and (b) show the XZ cross-sectional view of the restored images in the case of WF and pSIM systems, respectively. The WF images are restored using the expectation-maximization (EM) algorithm [15, 16] using the ideal (non-aberrated) PSF computed at 0 μm depth. The pSIM images are stored using the magnitude reconstruction technique [11], which is a demodulation technique that restores the image from the modulated section of the SIM raw data. Qualitatively, it is clear that, in the WF case, artifactual images are restored when there is a depth mismatch between the location of the object and the PSF that is used in the restoration. However, in the case of pSIM, the ring structure is well restored at all the depths, in contrast to the WF case. To show a quantitative comparison between these two cases, we computed the correlation coefficient between the XZ cross-sectional image of the true object and the restored images at different depths, reported on the images and also plotted in Fig. 2(c). From these values, we see that within the 100-μm imaging depth, the correlation coefficient value drops by 44% in the case of the conventional WF images, whereas in the case of pSIM it only changes by 12%. This observation suggests that, although the SIM imaging system suffers from depth-induced SA, its performance is more insensitive in the presence of SA compared to WF imaging. These results are supported by Ref. [10] in which authors also observed that pSIM images are less affected by depth-induced SA compared to the WF images. Due to this reduced effect of depth-induced SA in pSIM imaging, a single aberrated PSF can be used in the deconvolution process to account for the SA [10].

Additionally, to further quantify the effect of depth-induced SA on the SIM images, we compare the axial intensity profiles through the restored images in the case of pSIM taken along the red arrow shown in the image restored at the 0 μm depth. From the intensity profiles, one can conclude that the peak signals of the restored SIM images are decreased with the increase of the imaging depth. This results can be explained due to the fact that the increase of depth introduces a higher amount of depth-induced SA, which reduces the modulation contrast of the illumination pattern significantly, and consequently, there is a reduction of the restored signal [17, 18]. To finalize this quantitative analysis, we have calculated the isotropy ratio and the lateral and axial FWHM of the results show in panel (b) of Fig. 2, see Fig. 2(e). These values reveal that, the restored pSIM images remain undistorted in the lateral direction at different depth locations; however, in the axial direction the images start to deteriorate with the increasing depths.

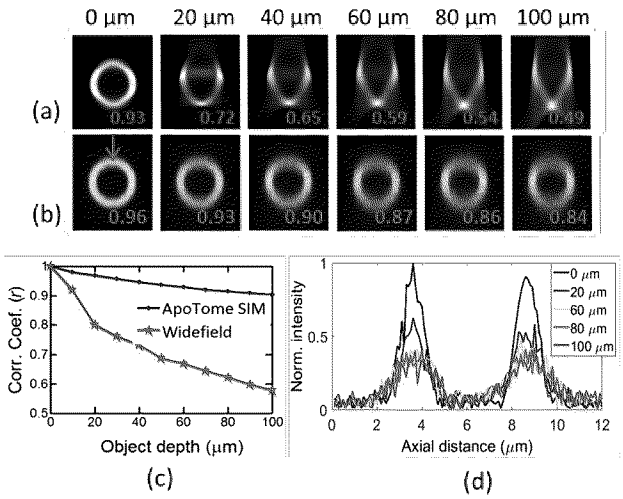


| Conv. ApoTome SIM | | | |
|---|---|---|---|
| Bead depths (µm) | Lateral FWHM (µm) | Axial FWHM (µm) | Ratio |
| 0 | 1.06 | 1.25 | 1.18 |
| 20 | 1.06 | 1.40 | 1.32 |
| 40 | 1.10 | 1.79 | 1.63 |
| 60 | 1.13 | 1.86 | 1.65 |
| 80 | 1.15 | 2.08 | 1.81 |
| 100 | 1.16 | 2.12 | 1.83 |

(e)

Fig. 2: Effect of depth-induced aberration in the case of pSIM images in the simulation. (a) Restored images using the ideal (e.g. non-aberrated) PSF from the conventional widefield images at different depths; (b) Simulated optical sectioned images obtained from pSIM-based images at different depths; (c) Correlation coefficient between the OS images at different depths; and (d) Axial profile through the OS images [panel (b)] at different depths. (e) Lateral and axial FWHM distance of the spherical shell thickness restored from different depths in the case of pSIM and their ratio.

## 4.2 Performance of the SQUBIC-WFE ApoTome SIM at different depths

To investigate the effect of depth-induced SA on the SQUBIC-WFE pSIM system, we simulated the corresponding SQUBIC-WFE forward image of the 6-µm spherical shell within the depth range 0 µm to 100 µm, and the restored images are shown in Fig. 3(b). As the SQUBIC-WFE PSF has a strong characteristic behavior [7], which distorts the intermediate images, the raw images need to be deconvolved before applying the magnitude demodulation in order to remove the effect of the SQUBIC-WFE PSF from the raw data. We have used the 2D SQUBIC-WFE PSF computed at the best focus to deconvolve the intermediate SQUBIC-WFE. For comparison purposes, the corresponding conventional pSIM images are also shown in Fig. 3(a). Qualitatively, it is observed that the axial shell thickness of the bead in the restored images for the SQUBIC-WFE pSIM system (Fig. 3b) are restored better compared to the ones obtained from the conventional pSIM system (Fig. 3a).

For a quantitative comparison, we again computed the correlation coefficients between the restored images (the values are reported in red in panels (a) and (b) of Fig. 3), the lateral and the axial shell thickness in terms of the FWHM distances, and the ratio between the axial width and the lateral width of the restored spheres. These values are shown in Fig. 3c. Here, we observe that within 100-µm imaging depth the correlation coefficients vary 12% in the case of pSIM images, whereas it only changes by 6% in the case of the SQUBIC-WFE pSIM system. Regarding the quantitative values reported in Fig. 3(c) compared to those in Fig. 2(d) we see that the results from both systems show similar accuracy in the restored lateral dimension of the shell; however, accuracy in the axial dimension and maintaining an isotropy in the restored dimensions of the bead is better in the SQUBIC-WFE pSIM system. Specifically, in the axial direction, the shell thickness at 100-µm depth below the cover slip is observed to be 2.12× of the manufacturer specified value (i.e. 1 µm) in the case of conventional pSIM, whereas it is observed to be 1.25× in the case of SQUBIC-WFE pSIM. This observation suggests that the SQUBIC-WFE pSIM system is less sensitive to SA.

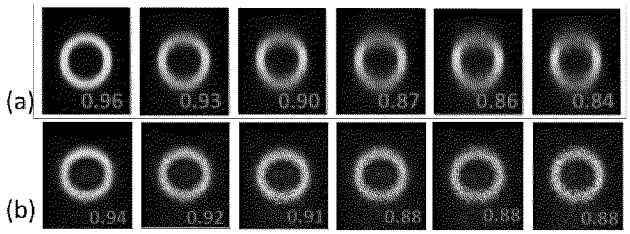


| SQUBIC-WFE ApoTome SIM | | | |
|---|---|---|---|
| Bead depths (μm) | Axial FWHM (μm) | Lateral FWHM (μm) | Ratio |
| 0 | 1.20 | 1.06 | 1.13 |
| 20 | 1.24 | 1.12 | 1.11 |
| 40 | 1.24 | 1.07 | 1.16 |
| 60 | 1.32 | 1.15 | 1.15 |
| 80 | 1.22 | 1.10 | 1.11 |
| 100 | 1.25 | 1.14 | 1.10 |

(c)

Fig. 3: Impact of the depth-induced SA in pSIM and SQUBIC-WFE pSIM implementation using simulated data. XZ cross-sectional views of (a) pSIM restored images, and (b) SQUBIC-WFE pSIM. The correlation coefficients are reported in red color for each restored image. (c) Performance metrics (lateral FWHM, axial FWHM and their ratio) computed from the restored images of the panel (a) for different depths.

## 4.3 Forward model evaluation

To evaluate the performance of the forward imaging model of the conventional and SQUBIC-WFE pSIM system, we compared simulated and experimental images of a 6-μm spherical shell with shell thickness equal to 1 μm. The XZ cross-sectional view of simulated and experimental raw SIM images for one of the three phase-shifted images in the case of conventional pSIM and SQUBIC-WFE pSIM are shown in Fig. 4 (a-d). From a qualitative comparison, we observe that the XZ-view images obtained from the experiments agree with the corresponding simulations. For a quantitative comparison, we have plotted axial intensity profiles through the arrows shown in Fig. 4 (b) and (d), which are shown in Fig. 4 (e) and Fig. 4 (f), respectively. The intensity profiles also demonstrate the agreement between the results obtained in the case of simulated and the experimental images.

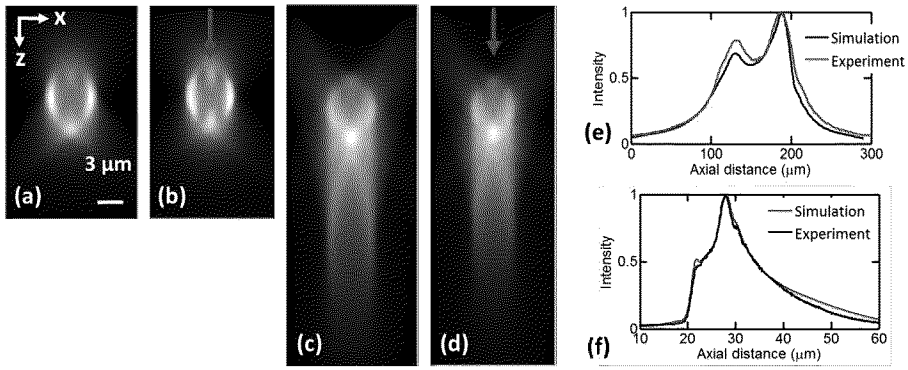


Fig. 4: Comparison between the simulated and the experimental raw pSIM images. XZ cross-sectional view image of the simulated and the experimental images and corresponding axial and lateral intensity profiles in the case of conventional (a-b) and SQUBIC-WFE (c-d) ApoTome® SIM system. (e-f) Normalized intensity profiles along the red arrow shown in (b) and (d).

## 4.4 Experimental image restoration

The impact of depth-induced SA on the pSIM images has been experimentally investigated by capturing the forward images of a test sample with 6 μm in diameter spherical shells located at three different depths (3, 22, and 55 μm) below the cover slip using both imaging paths (the conventional and SQUBIC-WFE pSIM) shown in Fig. 1. The illumination grating used in this experiment creates the fringe pattern at the sample plane, which has a frequency equal to $0.09f_c$. The restored images using the magnitude reconstruction method in the case of conventional and SQUBIC-WFE pSIM systems are shown in Fig. 5 (a) and (b), respectively. As in the case of the simulations, the experimental

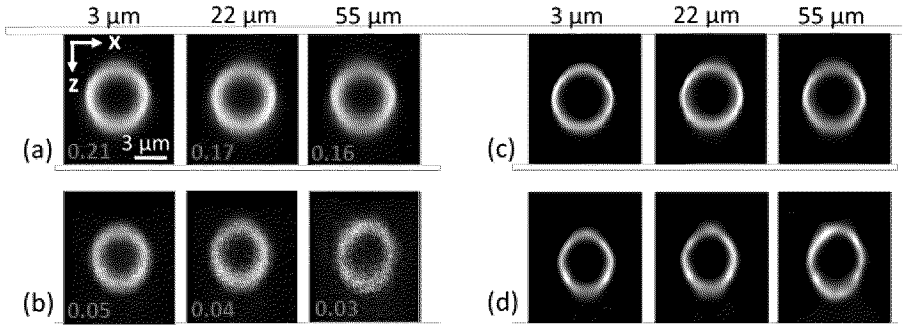


Fig. 5: Restoration of the image of the test object located at different depths below the cover slip captured using conventional and SQUBIC-WFE pSIM. XZ cross sections of the test object restored from depth locations 3 µm, 22 µm and 55 µm below the cover slip using the magnitude demodulation technique in the case of (a) conventional and (b) SQUBIC-WFE pSIM system. (c-d) Corresponding restored images using the method described in [17].

SQUBIC-WFE images are deconvolved before applying the magnitude demodulation. From a qualitative comparison, we observe that in the case of conventional pSIM, the images restored from different depth locations are similar. However, in the case of the SQUBIC-WFE pSIM system, the restored images show some artifact, particularly in the case of the bead at a 55-µm depth. These artifacts are related with the reduction of the $m_c$ values (shown in red at the bottom of the restored images Fig. 5 (a) and (b)) due to the SQUBIC PM use.

These experimental images were also restored using the deconvolution-based method described in [17, 18], which was demonstrated to obtain better optical sectioning even in the case where the modulation contrast is low in the presence of SA. The restored images using this method in the case of conventional and SQUBIC-WFE pSIM systems are shown in Fig. 5(c) and (d), respectively. The improvement in the restored images is clearly visible compared to the corresponding magnitude reconstruction based method (Fig. 5 (a) and (b)).

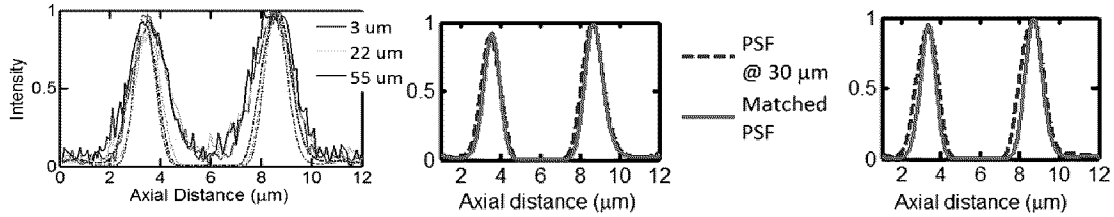


(a) (b) (c)

| Depth | Isotropy | | Axial shell thickness of the restored images | | | |
|---|---|---|---|---|---|---|
| | Conventional ApoTome SIM | SQUBIC ApoTome SIM | Magnitude Restoration | Deconvolution-based restoration | | |
| | | | | PSF @ 30 µm | PSF @ respective locations | SQUBIC WFE |
| 3 µm | 1.04 | 1.00 | 1.50 µm | 0.94 µm | 0.94 µm | 1.0 µm |
| 22 µm | 1.00 | 1.02 | 1.53 µm | 1.08 µm | 0.95 µm | 1.06 µm |
| 55 µm | 1.02 | 1.19 | 1.74 µm | 1.24 µm | 0.97 µm | 1.05 µm |

(d)

Fig. 6: Quantitative comparison of restored images of beads located at depth locations 3 µm, 22 µm, and 55 µm below the cover slip, respectively, in the case of pSIM. (a) Axial intensity profiles through the images restored using magnitude demodulation, and the deconvolution-based method described in [17, 18]. Intensity profile comparison, when the pre-aberrated PSF and the PSF at the respective depth locations are used in the restoration, while the beads are at: (b) 22 µm, and (c) 55 µm depths. (d) Summary of the axial shell thickness in different cases.

For a quantitative comparison, the axial intensity profiles through the center of the restored images in the case of conventional pSIM, and the deconvolution-based methods are shown in Fig. 6. From Fig. 6 (a), we observe that, in the case of the deconvolution-based method (where an aberrated PSF at 30 μm depth is used to account for the pre-aberration present in our system [7]), the axial shell thickness becomes closer to the nominal value (i.e. 1 μm). For a comparative study, we also restored the images from depths 22 μm and 55 μm using a PSF at their respective depth locations. The intensity profiles in the case of bead at depths 22 μm, and 55 μm are shown in Fig. 6 (b) and (c), respectively, where we see that the axial shell dimension is restored with less error if a single PSF at the respective depth location is used in the restoration (see the table in Fig. 6 (d)). From the table we also see that both systems perform similarly to restore the isotropic shape (measured in terms of the ratio of the axial and lateral peak distances between two lobes) of the spherical shell. The shell thickness in the case of SQUBIC-WFE pSIM is also reported in this table (Fig. 6(d)), which shows that the shell thickness is adequately restored while using the same PSF (ideal SQUBIC-WFE pSIM PSF at 0 μm depth) for the deconvolution.

## 5. CONCLUSION

In this paper, the performance of pSIM in the presence of depth-induced SA was investigated. A hybrid SQUBIC-WFE pSIM system was presented and its performance was investigated by restoring images of spherical shells located at different depths below the cover slip. Our simulations show that the pSIM system is less sensitive to depth-induced SA compared to the conventional WF imaging system, which is consistent with a previous observation [10]. For example, over a 100 μm imaging depth, the images restored in the case of the conventional WF system show a variability of 44%, whereas, in the case of conventional SIM, the variability reduces to 12%. The conventional SIM restored images show axial distortion, which increases with the increase of imaging depth. We observed that, in the axial direction, the shell thickness becomes larger than the true thickness of 1 μm as the depth increases. If a PSF at the approximate depth location is used in the deconvolution-based SIM restoration method then a better restoration can be achieved. In the case of SQUBIC-WFE pSIM, the same non-aberrant PSF can be used to restore images of beads located at different depths because of its insensitivity to depth-induced SA. However, the restoration in the WFE system is more challenging due to the reduction in the fringe contrast because of the SQUBIC PM, which results in artifacts in the restored image of beads at a higher depth. Hence, in the case of the pSIM system, for the particular imaging conditions and simple test sample investigated in this study, we show that deconvolution-based SIM restoration with an aberrated PSF computed at an approximate depth equal to the center of the imaging volume below the cover slip could render a result with adequate accuracy. Further investigation of possible benefits of SQUBIC-WFE SIM for other imaging conditions is still needed.

## Acknowledgements

This work is supported by the National Science Foundation (IDBR award DBI-1353904, PI: CP) and the University of Memphis. Authors thank L. H. Schaefer (Advanced Imaging Methodology Consultation, Ontario, Canada) for Matlab code used in the pSIM simulation. G. Saavedra and M. Martinez-Corral acknowledge funding from Ministerio de Economia y Competitividad, Spain (Grant DPI2015-66458-C2-1-R) and Generalitat Valencia (Grant PROMETEOII/2014/072). J. Sola-Pikabea acknowledges predoctoral funding from Generaltat Valenciana (ACIF/2016/296).

## References

[1] C. Preza, and J.-A. Conchello, "Depth-variant maximum-likelihood restoration for three-dimensional fluorescence microscopy," Jornal of Optical Society of America A, 21, 1593-1601 (2004).

[2] M. J. Booth, "Adaptive optics in microscopy," Philosophical Transactions of the Royal Society A-Mathematical Physical and Engineering Sciences, 365, 2829-2843 (2007).

[3] M. Arigovindan, J. Shaevitz, J. McGowan *et al.*, "A parallel product-convolution approach for representing the depth varying point spread functions in 3D widefield microscopy based on principal component analysis," Optics express, 18(7), 6461-6476 (2010).

[4] S. Yuan, and C. Preza, "Point-spread function engineering to reduce the impact of spherical aberration on 3D computational fluorescence microscopy imaging," Optics Express, 19(23), 23298-23314 (2011).

[5] G. Saavedra, I. Escobar, R. Martínez-Cuenca *et al.*, "Reduction of spherical-aberration impact in microscopy by wavefront coding," Optics Express, 17(16), 13810-13818 (2009).

[6] N. Patwary, H. Shabani, A. Doblas *et al.*, "Experimental validation of a customized phase mask designed to enable efficient computational optical sectioning microscopy through wavefront encoding," Applied Optics, 56(9), D14 (2017).
[7] N. Patwary, S. V. King, G. Saavedra *et al.*, "Reducing effects of aberration in 3D fluorescence imaging using wavefront coding with a radially symmetric phase mask," Optics Express, 24(12), 12905-12921 (2016).
[8] W. T. Cathey, and E. R. Dowski, "New paradigm for imaging systems," Applied Optics, 41(29), 6080-6092 (2002).
[9] C. Preza, "Simulating structured-illumination microscopy in the presence of spherical aberrations," SPIE BiOS, 79040D-79040D (2011).
[10] C. Preza, L. Schaefer, D. Schuster *et al.*, "Impact of spherical aberration on structured-illumination microscopy," In Focus on microscopy, Singapore, April 1-4, (2012).
[11] L. H. Schaefer, D. Schuster, and J. Schaffer, "Structured illumination microscopy: artefact analysis and reduction utilizing a parameter optimization approach," Journal of microscopy, 216(2), 165-174 (2004).
[12] M. A. A. Neil, R. Juskaitis, and T. Wilson, "Method of obtaining optical sectioning by using structured light in a conventional microscope," Optics Letters, 22, 1905-1907 (1997).
[13] A. Doblas, A. Dutta, G. Saavedra *et al.*, "Tradeoff between insensitivity to depth-induced spherical aberration and resolution of 3D fluorescence imaging due to the use of wavefront encoding with a radially symmetric phase mask " SPIE, BiOS, (2018), accepeted.
[14] S. F. Gibson, and F. Lanni, "Experimental test of an analytical model of aberration in an oil-immersion objective lens used in three-dimensional light microscopy," Journal of the Optical Society of America A-Optics Image Science and Vision, 9, 54–66 (1992).
[15] J.-A. Conchello, "Superresolution and convergence properties of the expectation-maximization algorithm for maximum-likelihood deconvolution of incoherent images," Journal of the Optical Society of America A, 15(10), 2609-2619 (1998).
[16] J.-A. Conchello, and J. G. McNally, "Fast regularization technique for expectation maximization algorithm for optical sectioning microscopy," Electronic Imaging: Science & Technology, 2655, 199-208 (1996).
[17] N. Patwary, A. Doblas, and C. Preza, "Image restoration approach to address reduced modulation contrast in structured illumination microscopy," Biomedical optics express, (under review), (2017).
[18] N. Patwary, A. Doblas, and C. Preza, "Computational approach to address reduced modulation contrast in structured-illumination microscopy," in Imaging and Applied Optics , OSA Technical Digest (online), JTu5A.9, (2017).